Measurement of Ionospheric Scintillation Parameters From SAR Images Using Corner Reflectors

Christopher R. Mannix, David P. Belcher, and Paul S. Cannon

***Abstract*— Space-based low-frequency (L-band and below) synthetic aperture radar (SAR) is affected by the ionosphere. In particular, the phase scintillation causes the sidelobes to rise in a manner that can be predicted by an analytical theory of the point spread function (PSF). In this paper, the results of an experiment, in which a 5 m corner reflector on Ascension Island, was repeatedly imaged by PALSAR-2 in the spotlight mode are described. Many examples of the effect of scintillation on the SAR PSF were obtained, and all fit the theoretical model. This theoretical model of the PSF has then been used to determine two ionospheric turbulence parameters p and C_kL from the SAR PSF. The values obtained have been compared with those obtained from simultaneous GPS measurements. Although the comparison shows that the two measures are strongly correlated, the differing spatial and temporal scales of SAR and GPS make exact comparison difficult.**

***Index Terms*— Ionosphere, ionospheric electromagnetic propagation, synthetic aperture radar**

I. Introduction

THE ionosphere imposes a number of effects on the signals and images collected by space-based L- and P-band synthetic aperture radars (SARs), including Faraday rotation, image shift, defocusing, and amplitude modulation. A recent short review [1] provides a useful collation of much of the contemporary literature.

Previous studies of the impact of the ionosphere on SAR systems have primarily addressed the effects of Faraday rotation [1] and [2]. However, defocusing and reduction in image contrast due to small-scale ionospheric irregularities has also been recognized. That this is a very real problem was demonstrated by [3], and a series of papers [4]–[6] has sought to relate the SAR image statistics and point spread function (PSF) to the strength of ionospheric turbulence. A recent paper [7] has also explored how L-band Global Navigation Satellite System (GNSS) signals can be used as a proxy for L-band SAR signals and explored how small-scale irregularities affect the signal correlation distances. The latter paper builds on earlier work [8] using V/UHF signals to evaluate SAR performance.

Manuscript received September 6, 2016; revised December 16, 2016, April 11, 2017, and June 15, 2017; accepted June 20, 2017. Date of publication October 10, 2017; date of current version November 22, 2017. This work was supported by the U.K. Engineering and Physical Sciences Research Council under Grant EP/I013601/1. *(Corresponding author: David P. Belcher.)*

The authors are with the University of Birmingham B15 2TT, U.K. (e-mail: d.belcher@bham.ac.uk).

Color versions of one or more of the figures in this paper are available online at http://ieeexplore.ieee.org.

Digital Object Identifier 10.1109/TGRS.2017.2727319

A few authors have also explored the inverse problem of how a space-based SAR might be used to image large-scale features in the ionosphere and again [1] provides a useful review of the literature. For example, [9] discussed how the ionospheric phase advance and group delay might be measured by interferometric techniques and [10] developed a technique using PALSAR-1 [11] polarimetric data to generate 2-D ionospheric images.

Measuring and imaging the small-scale irregularities, often quantified through the integrated strength of (irregularity) turbulence parameter C_kL using a SAR has received far less attention. This paper, being an extension of preliminary analysis reported in [12], seeks to rectify this. It does this by adopting the theoretical framework of [6], which describes how ionospheric turbulence affects the SAR PSF, to infer C_kL. The associated experimental technique involves imaging a trihedral corner reflector (CR) to determine the PSF—such targets are typically used for radiometric calibration and image quality analysis of SAR systems [13]. To facilitate this, two CRs were deployed on Ascension Island (in the South Atlantic) under the equatorial ionosphere, where ionospheric scintillation occurs. PALSAR-2 [14], [15] was then used to image the island, including the CRs on multiple occasions.

II. Theory

A. Turbulent Ionosphere

Under benign ionospheric conditions, the free electron density N_e is horizontally homogenous with a smooth vertical profile and a peak ionization at 300–350 km altitude. However, when the ionosphere is disturbed significant deviations in N_e can occur, the cause of which is turbulence in the ionosphere. These irregularities in electron density in turn cause scintillation of electromagnetic waves passing through the ionosphere. Although these irregularities are random they can be described by a power law power spectrum. The electron density irregularities are generally elongated along the geomagnetic field lines, so the power spectrum is anisotropic.

Each deviation δN_e introduces a phase change, $\delta\phi = r_e\lambda\delta N_e$ where r_e is the classical electron radius, and λ is the wavelength. The total phase change is given by the integral over all of the irregularities along the propagation path and for convenience, the impact of the 3-D distribution of irregularities can be represented as a 2-D phase screen located at a fixed altitude. The power spectral density (PSD)

of the phase change imposed by the screen is [6], [16]

$$\mathrm{PSD}_{\phi}(\kappa) = T'\left(\sqrt{\kappa_0^2 + \kappa^2}\right)^{-p} \tag{1}$$

where $\kappa = 2\pi/x_p$ is the spatial wavenumber corresponding to a distance x_p along the phase screen, p is the spectral index of the irregularities in the phase screen, and $\kappa_0 = 2\pi/l_0$ is the outer scale wavenumber, l_0 being the outer scale size of the irregularites. The value of T' is given by

$$T' = \frac{r_e^2\lambda^2 G C_k L \sec\theta\sqrt{\pi}\,\Gamma(p/2)}{(2\pi)^2\Gamma((p+1)/2)}\kappa_{1\,\mathrm{km}}^{p+1} \tag{2}$$

where C_kL is a compound parameter being the integrated strength of turbulence at 1 km scale size, $\sec\theta$ scales the path length to an incidence angle θ, G is a geometric factor that depends on the irregularity anisotropy [see 17, eq. (A10)] with reference to the geomagnetic field. The latter was calculated from the International Geomagnetic Reference Field [18]. $\kappa_{1\,\mathrm{km}} = 2\pi/1000$ (rad m^{-1}).

B. One-Way Phase Spectrum

The phase modulation of a signal transmitted from a satellite is determined by the intersection of the line-of-sight to a fixed ground point with the phase screen. The intersection point is known as the ionospheric penetration point (IPP), the ionosphere having an assumed height which has been chosen to be 350 km in this paper. As the satellite moves along its track the IPP moves along the phase screen, modulating the phase received at a fixed ground point.

In practice, the data are recorded by a fixed ground receiver (often a GPS receiver) as a function of time and consequently the spectrum is expressed as a function of frequency f. This frequency spectrum is not only dependent on the characteristics of the screen, but is also dependent on the velocity of the IPP which is itself dependent on both the velocity of the satellite and the drift velocity of the ionosphere. Moreover, the anisotropy must be accounted for and this can be achieved by using an effective velocity v_{eff} rather than the actual velocity of the IPP [17]. The received phase power spectrum can be expressed as

$$\mathrm{PSD}_{\varphi}(f) = T_{\mathrm{GPS}}\left(\sqrt{f_o^2 + f^2}\right)^{-p} \approx T_{\mathrm{GPS}} f^{-p} \tag{3}$$

where f_o is the outer scale frequency ($f_o = v_{\mathrm{eff}}/l_o$). The approximate form is valid when f_o is sufficiently small that it can be neglected. For $v_{\mathrm{eff}} = 100$ ms^{-1} and $l_o = 10$ km (choices which will be substantiated later) this approximation is valid down to $\sim$0.05 Hz.

The value of T_{GPS} is given by adapting [16, eq. (18)]

$$T_{\mathrm{GPS}} = \frac{r_e^2\lambda^2 G C_k L \sec\theta\sqrt{\pi}\,\Gamma\ (p/2)}{\Gamma\ ((p+1)/2)10^6}\left(\frac{v_{\mathrm{eff}}}{1000}\right)^{p-1} \tag{4}$$

where [19] has been used to relate the strength of turbulence C_S to the more commonly used height-integrated strength of turbulence, C_kL [a parameter of the Wideband Model (WBMOD)] as

$$C_sL = \left(\frac{2\pi}{1000}\right)^{p+1} C_kL. \tag{5}$$

Thus, by measuring the received power spectrum from, for example, a GPS receiver, it is possible to derive both p and C_kL for that part of the phase screen through which the ray path passes.

C. Point Spread Function

As the radar satellite flies along its track, the IPP moves along the phase screen, modulating the phase to a point target, such as a CR. For a monostatic radar, the correlation distances and round trip time delays are such that the two-way phase is twice the one-way phase.

The PSF is given by the Fourier transform of the radar data along the synthetic aperture and may be closely approximated by the sum of the ideal SAR impulse response (in the absence of phase errors) plus the sidelobe function. Belcher and Rogers [6] shows that the sidelobes η can be determined from the phase PSD and that their ensemble average shape $\langle|\eta(r)|^2\rangle$ as a function of resolution cell r is

$$\langle|\eta(r)|^2\rangle = T_{\mathrm{SLF}}\left(\sqrt{r_0^2 + r^2}\right)^{-p} \tag{6}$$

with the mainlobe defined to be at $r = 1$. The parameter $r_0 = L_{\mathrm{SA}}/\gamma\, l_o$ is the ratio of the synthetic aperture length to the ionospheric outer scale size l_o, scaled by γ the ratio of the satellite velocity to the effective velocity of the radar IPP, v_{eff}. The value of T_{SLF} is given in [5] as

$$T_{\mathrm{SLF}} = 4\gamma\,\kappa_C^{1-p} G C_k L \sec(\theta)(r_e\lambda_0)^2 \frac{\sqrt{\pi}\,\Gamma\left(\frac{p}{2}\right)}{(2\pi)^2\Gamma\left(\frac{p+1}{2}\right)}\kappa_{1\,\mathrm{km}}^{p+1} \tag{7}$$

where $\kappa_C = 2\pi\,\gamma\,/L_{\mathrm{SA}}$ and λ_0 is the wavelength at the radar center frequency and G is defined in (2). This equation has obvious similarities to (4).

Practically, we also see that a fit of the sidelobe PSF to equation (6) gives T_{SLF} and p which in turn, with knowledge of the propagation geometry and effective velocity, gives C_kL from (6).

III. Experiment

Full details of the experiment design and relevant parameters are contained in [12], but essentially images of CRs, from which the PSF could be measured, were obtained using PALSAR-2. This is an L-band space-based SAR carried by the Advanced Land Observing Satellite 2 (ALOS-2). The radar operates at 1257.5 MHz, and all of the PALSAR-2 data used in this paper correspond to the radar operating in spotlight mode providing 1 m (along track) and $\sim$2 m (cross track) resolution. The orbit of ALOS-2 is sun synchronous with a 14-day repeat cycle.

Two CRs, with side length 5 m, were deployed on Ascension Island in the South Atlantic Ocean (7.9°S, 14.8°W). The CR locations are shown in Fig. 1 as red triangles—that on the west side of the island looked approximately west and that on the east side of the island looked approximately east. The CRs were oriented to point toward the average ascending node pass, which varies according to the range to the satellite. The deployment allowed measurements of the PSF to be made

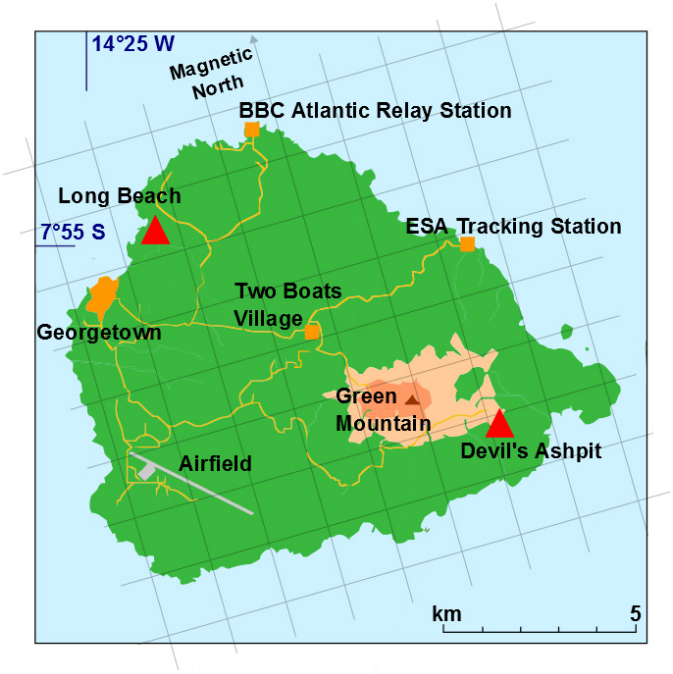

Fig. 1. Map of Ascension Island.

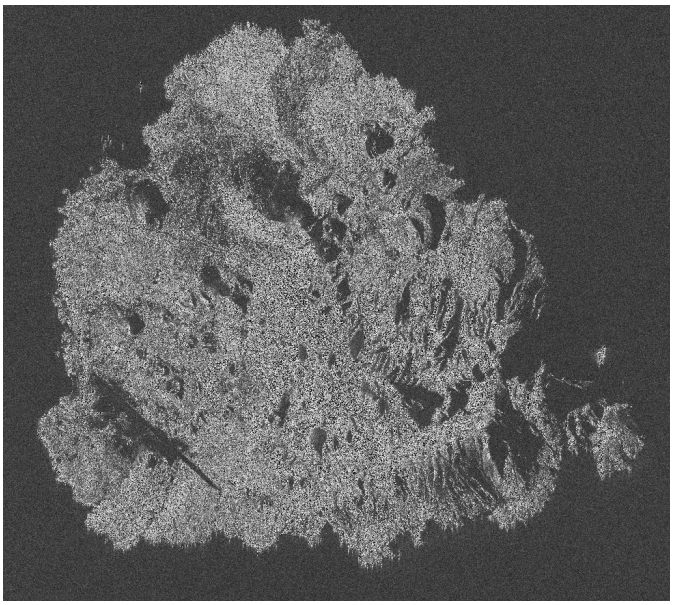

Fig. 2. Whole island image (August 18, 2014, no scintillation).

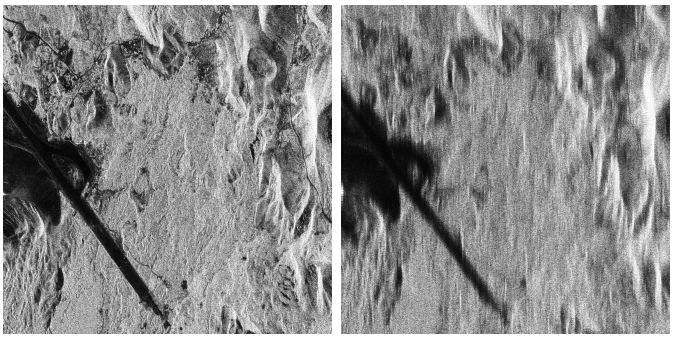

Fig. 3. L-band PALSAR-2 images of the runway and surrounding terrain on Ascension Island. (Left) No scintillation. (Right) Moderate scintillation.

for both east and west looking PALSAR-2 passes. The first data collect occurred on August 18, 2014 close to the start of the Atlantic sector scintillation season and the last during April 2015.

Ascension Island is located within the ionospheric equatorial region. Here, the electron density irregularities that cause scintillation mainly form in the postsunset hours between 21 and 00 local time (LT) [20] but with some scintillation effects before and after these times. PALSAR-2 images Ascension Island between 00 LT and 02 LT, which, while not ideal, still provides good opportunities for measuring scintillation effects.

Ascension Island was imaged by PALSAR-2 on a number of different ground tracks with various slant ranges and incidence angles. The CRs were set to provide a maximum radar cross section (RCS) at an incidence angle of 45°, but the RCS remains high between 15° and 75°. Since PALSAR-2 imagery is formed at incidence angles between 8° and 70°, the response from the CRs is easily identifiable in every image.

The variety of propagation geometries leads to different values for the synthetic aperture length L_{SA}, upon which the quantity r_0 (6) is dependent. This value is calculated as

$$r_0 = \frac{L_{\mathrm{SA}}}{\gamma\, l_0} = \frac{R\lambda_0}{2\rho_{\mathrm{az}}} \times \frac{1}{\gamma\, l_0} \tag{8}$$

where ρ_{az} is the azimuth resolution of the SAR. The value for the outer scale size (l_0) is fixed at 10 km [21] which reduces the number of free parameters in later analysis and the azimuth resolution (ρ_{az}) and radar wavelength (λ_0) are 1 and 0.23 m, respectively. The chosen outer scale is consistent with the WBMOD model, the scientific background of which is described in [22]. WBMOD used a value of 10 km in early and 6 km in later implementations but maintained consistency with the underlying measurements by changing the ratio of the cross-field to along-field elongation from 30 to 50. Note, however, that it is not the value of the elongation or the outer scale that matters, but rather their product because it is the latter which dictates the propagation for a polar orbiting, cross-field looking radar.

IV. Island Images

A total of 76 images of the island were collected, of which 61 were collected against the westward looking CR and 15 were collected against the eastward CR. The eastward looking CR is better for observing scintillation effects as the SAR looks at an ionosphere at an earlier local time. The data set provided a good sampling of a wide variety of ionospheric activity.

A whole island image is shown in Fig. 2 with just the south–west corner, including the island runway, shown in Fig. 3. The latter illustrates the impact of the ionospheric irregularities on the performance of the radar (which will be quantified through the PSF). On the left is an image generated on October 21, 2014 when the ionosphere was benign with S_4 measured on the nearest GPS path equal to 0.05. On the

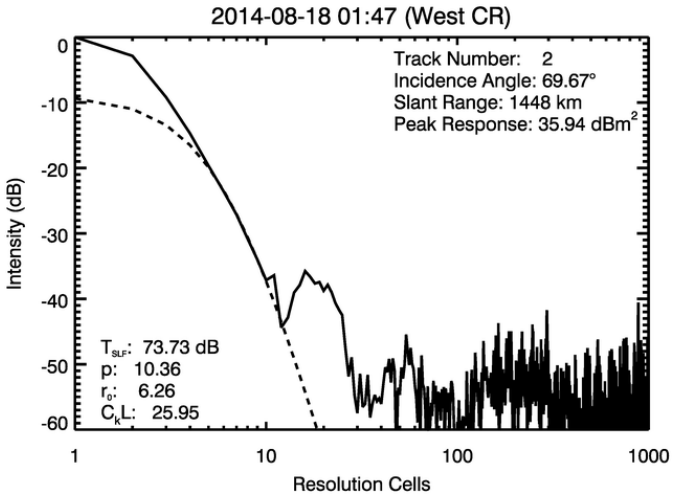

Fig. 4. West CR PSF, August 18, 2014 01:47.

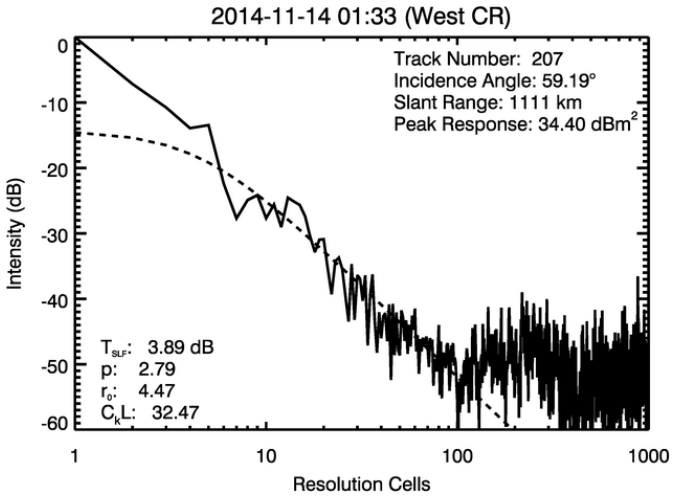

Fig. 5. West CR PSF, November 14, 2014 01:33.

right is an image generated on December 16, 2014 when the ionosphere was disturbed with S_4 measured on the nearest GPS path equal to 0.32.

V. PSF Measurement Results

The PSF was measured by identifying the CR in the image, and extracting a strip of intensity values in the along-track direction, centered on the mainlobe (as determined by the pixel with the highest intensity). The left and right halves of the sidelobe function were averaged to produce a one-sided distribution.

The theoretical SAR sidelobe function when subjected to ionospheric disturbance (7) was fitted to the sidelobes of the measured PSF. For curve fitting purposes the sidelobes were defined as being those points that were no more than 35 dB below the mainlobe peak (to avoid contamination by clutter), and at least three resolution cells away from the mainlobe peak resolution cell (to avoid contamination by the mainlobe). The constant of proportionality T_{SLF} and the spectral slope p were the free parameters of the fit, which was performed by minimizing the mean square error statistic. The results are normalized to the peak of the mainlobe which varies from plot to plot.

Fig. 4 shows an example of the measured PSF when unaffected by ionospheric scintillation. There is a clear mainlobe, with clutter at least 35 dB below it. The rapid fall off of the measured sidelobes and the high values of the fitted p both illustrate that the ionosphere has had a negligible impact on the PSF.

In contrast, Fig. 5 shows ionospheric degradation of the PSF. The fitted sidelobe function (dashed line) gives $T_{\mathrm{SLF}} = 3.89$ dB and $p = 2.79$ and the corresponding value of $\log_{10} C_k L$ is 32.47. Both the values of p and $\log_{10} C_k L$ are well within the expected range.

The majority of the phase spectral index values lay between 1 and 3, with a median value of 2.5 which is consistent with the expected value [23]. When there is no ionospheric degradation the PSF is characterized by a well-defined mainlobe and sidelobes, dictated by the radar design, which fall off rapidly to a clutter floor at approximately 35 dB below the mainlobe peak. The latter gradient is much higher than when the ionosphere is disturbed. For automatic processing, a threshold was chosen to delineate between the disturbed and undisturbed regimes. This was set, by inspection at $p = 5$. In summary, large p values are indicative of little to no ionospheric disturbance and setting a threshold at $p = 5$ (also consistent with the GPS measurements reported in the following section) reduced the data set from 76 to 60 points. That is 79% of the time there were discernible ionospheric effects.

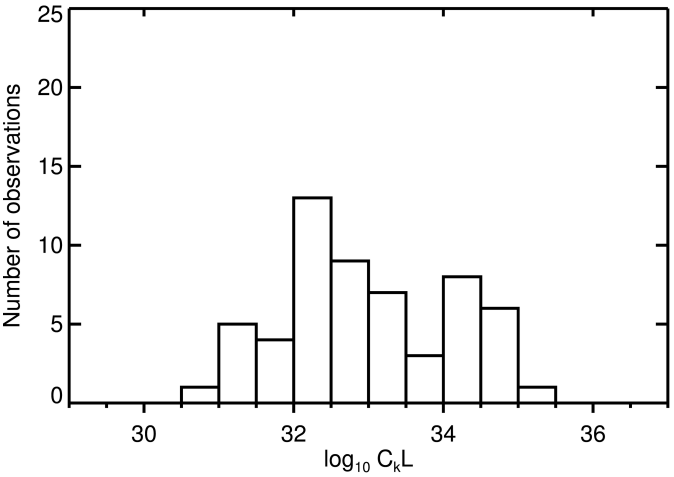

Fig. 6. Histogram of $C_k L$ values from fit of theoretical sidelobe function to measured CR response ($p \leq 5$).

Of these points $\log_{10} C_k L$ ranged from 30.7 to 35 (Fig. 6), values consistent with those predicted by WBMOD for the postsunset period at Ascension Island (see [24]).

VI. Comparison With GPS $C_k L$ Results

The $C_k L$ values derived from the fit to the SAR PSF were also compared to those obtained from simultaneous and independent GPS measurements with IPPs as close as possible.

For the comparison, 50 Hz GPS carrier phase data from a dual frequency, Septentrio PolaRx4 PRO GNSS receiver with an external Rubidium clock were used. This was located at

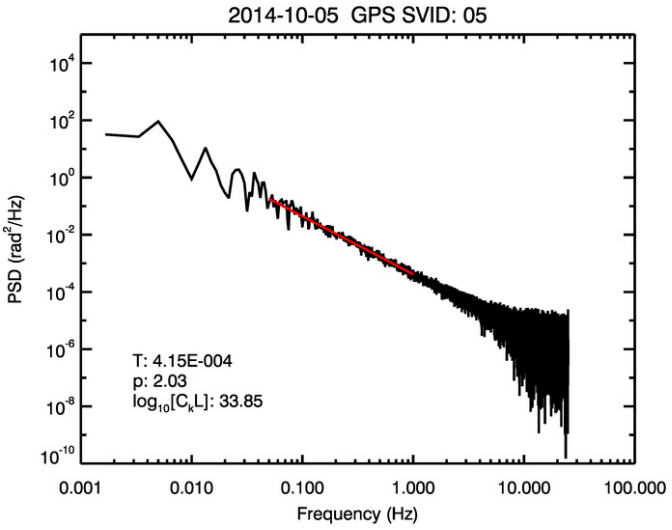

Fig. 7. GPS phase PSD–GPS single vehicle identification 5—October 5, 2014.

the European Space Agency Tracking Station (Fig. 1) 7.7 km from the west CR and 4.2 km from the east CR.

The raw GPS data were processed in the manner described by [7]. Slant total electron content (TEC) values were calculated by differencing the raw L1 and L2 phase, and these were converted to an equivalent phase (advance) time series. This removed the effects of the satellite motion. Further, the quadratic and linear components were removed from the phase time series, a procedure analogous to that which would be performed during the SAR imaging process to remove the effects of the change in the range to the target on the returned signal phase.

A linear log–log fit, according to (3), to the power spectrum between 0.05 and 1 Hz (Fig. 7) was performed to determine values for T_{GPS} (the value of the power spectrum at 1 Hz) and the corresponding GPS spectral slope p.

In doing so the effective scan velocity, v_{eff} of the GPS ionospheric pierce point (IPP) was calculated for each data point using the satellite position and velocity. This took into account the ionospheric anisotropy, with irregularity elongation factors of unity along the magnetic east–west axis, and ~30 along the north–south axis [22]. Given that no drift data were being collected on the island the ionospheric drift velocity was fixed at 100 ms^{-1} west to east. [20], [25] suggest velocities between 100 and 200 ms^{-1} for the premidnight hours, but because these measurements were made postmidnight a low, rather than high, nominal value was chosen.

The GPS IPP effective velocity also dictated the averaging period used in the power spectra. The requirement here is to have an aperture similar to the spotlight PALSAR-2 measurement, being ~60 km. As such, a longer averaging period than the more typical 30 s or 60 s (see [26]) was required. This was set at 600 s by assuming that the effective velocity is dominated by the 100 ms^{-1} ionospheric drift velocity. In each case, the phase time series was centered at the time at which PALSAR-2 was broadside to the center of the corresponding image.

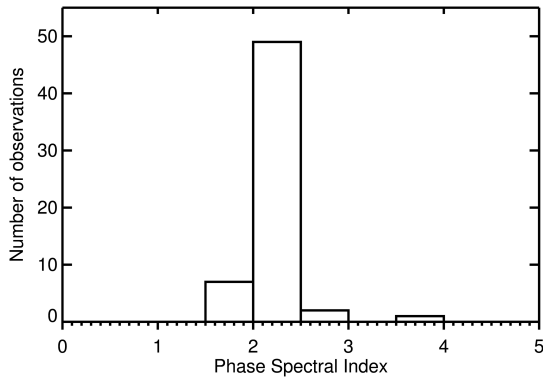

Fig. 8. Histogram of p values from fit to measured GPS phase PSD.

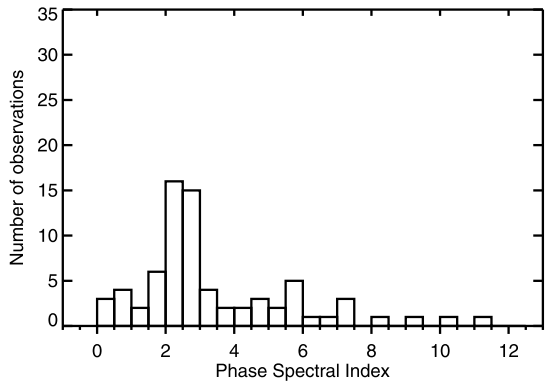

Fig. 9. Histogram of p values from fit to measured CR phase PSD.

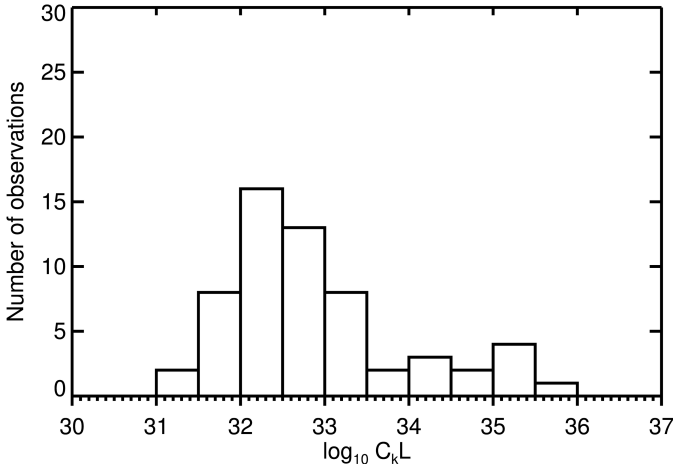

Fig. 10. Histogram of $C_k L$ values from fit to measured GPS phase PSD.

In the following, the subscripts CR and GPS will be variously used to distinguish the two categories of data. There was very little variation in the slope of the fitted line across the 60 cases, with the great majority of p_{GPS} values lying between 2 and 3 (Fig. 8). The p_{CR} values were much more spread out, but similarly the greatest density of values was found between 2 and 3 (Fig. 9). For $p_{\mathrm{CR}} < 5$, the $C_k L_{\mathrm{GPS}}$ distribution (Fig. 10) was similar, but clearly not identical to $C_k L_{\mathrm{CR}}$ distribution (Fig. 6).

Fig. 11 is a point-by-point comparison of $\log_{10} C_k L$ for those points, where the slope was less than five, and also

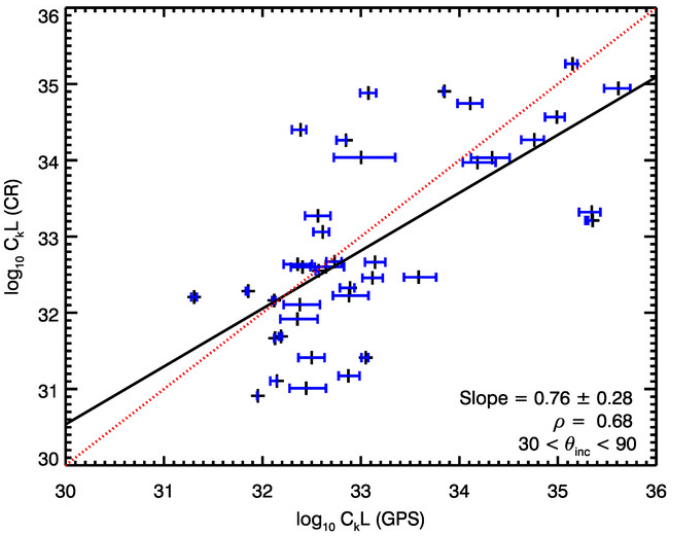

Fig. 11. Comparison of CR and GPS $C_k L$ values (CR $p \leq 5$, incidence angles $> 30°$).

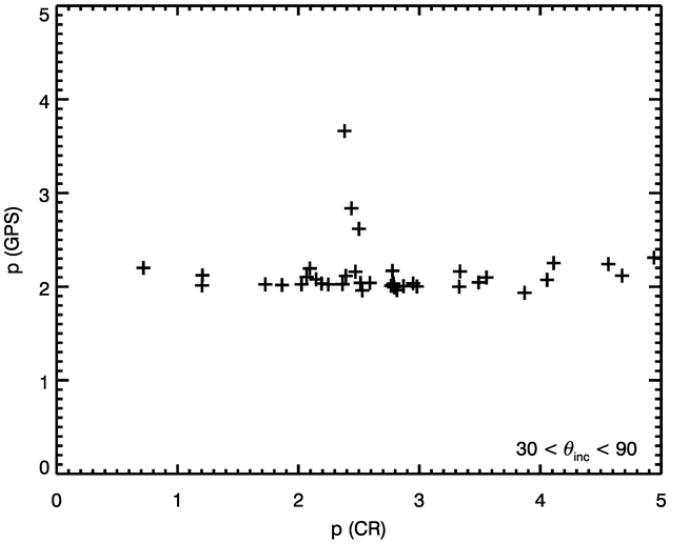

Fig. 12. Comparison of CR and GPS phase spectral index, p-values (600-s phase power spectrum).

where the incidence angle was above 30°. The latter requirement was imposed to ensure that the signal-to-clutter ratio was sufficiently high. The horizontal error bars describe the impact of varying the unknown ionospheric drift velocity from 50 to 150 ms^{-1}. The least-squares fit to a linear relationship between the two has a linear slope (solid black line) of 0.76 ± 0.28 (0.80 from a least absolute deviation fit) with a correlation coefficient of 0.68. The dotted line shows the $x = y$ slope for comparison.

While there is clearly some agreement, the results were somewhat disappointing. Some of the disagreement is very likely due to the IPP separation between the GPS and radar ray paths which varies between 100 and 500 km being many multiples of the outer scale. No relationship could be found between the IPP separation distance (either the absolute or the east–west component) and the point by point differences in $C_k L$.

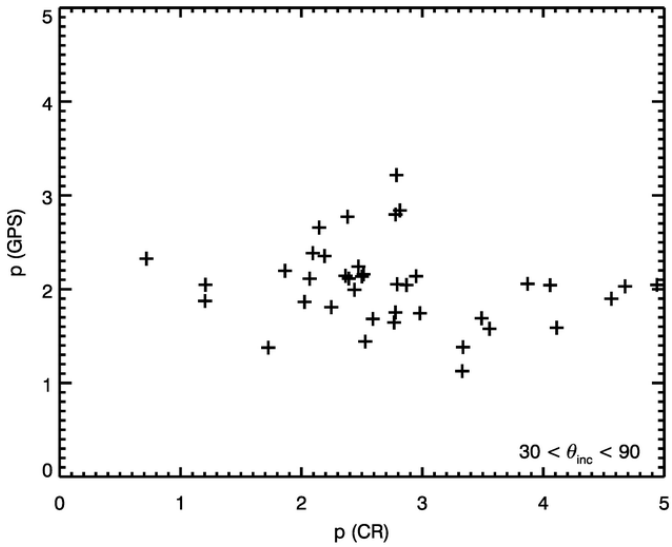

Fig. 13. Comparison of CR and GPS phase spectral index, p-values (30-s phase power spectrum).

The systematic error appears to be at least partly due to the different spatial and temporal scales over which the CR and GPS measurements were made. This is illustrated by a comparison of Figs. 12 and 13. Fig. 12 shows an intercomparison of the spectral indices (corresponding to Fig. 11) between the CR and GPS data using a 600-s GPS averaging period, and Fig. 13 shows the same comparison using a more conventional 30-s GPS averaging period. Evidently the long 600 s (corresponding to ~60 km) GPS integration has averaged out the extreme values. Only by reducing the integration time to 30 s, can these extreme (low and high) p values be seen. Similar averaging down also occurs for the GPS estimates of $C_k L$ (Fig. 10). In contrast, because the CR measurements (Fig. 6) were made within a short period of ~10 s, there was little opportunity for temporal variation and there was little averaging.

VII. Discussion

This paper has demonstrated that the L-band PALSAR-2 satellite can be used to estimate the ionospheric integrated strength of turbulence parameter $C_k L$ by measuring the PSF of a CR and applying the theory first described in [6].

This new technique provides a snapshot in time based on a ten-second average rather than the thirty or sixty-second average typically required by GNSS based techniques. This is extremely important in the equatorial regions where the evening west–east ionospheric drift speed, in which the irregularities are embedded, is often 100 ms^{-1} and sometimes higher.

Of course, even though the SAR CR measurements only take 10 s to collect, the corresponding synthetic aperture is ~60 km long corresponding to ~30 km in the phase screen. Fortunately, because the satellite is in a near polar orbit, and because equatorial irregularities are elongated north–south the poor north–south resolution is not an issue.

The results presented in this paper indicate a CR sensitivity down to a $\log C_k L$ of $\sim$31. While discussing the experimental sensitivity it is also important to recall two assumptions. The first is that these measurements were made using PALSAR-2 in its highest resolution mode. As a consequence, the CR stands out against the background. If a coarser resolution mode were used the signal-to-clutter ratio would be reduced, with a corresponding increase in the minimum $C_k L$ that can be measured. Second, it is important to remember that the theory on which this inverse approach is founded assumes weak scattering. Consequently, in addition to there being a sensitivity controlled lower limit to the technique, there is also an upper limit. The same of course applies to the GPS measurements. The crossover from weak to strong scatter may occur around $C_k L = 5 \times 10^{34}$ [27] for L-band systems.

VIII. Conclusion

A theoretical model has been used to determine two ionospheric parameters p and $C_k L$ from the PSF associated with an L-band SAR. The values obtained have been compared with those obtained from simultaneous GPS measurements. Although the comparison shows that these two measures are strongly correlated, the differing temporal and spatial resolutions of SAR and GPS make exact comparison difficult.

The validation and testing of this new technique is in its early stages but it appears to offer a number of new scientific opportunities. For example, an array of cheap, passive CRs distributed over ten or more kilometres might enable the variation of ionospheric irregularity statistics to be remotely inferred. An alternative approach to measuring the strength of turbulence using space-based SAR by measuring the change in clutter parameters when the ionosphere is disturbed is the subject of another paper [28].

Acknowledgment

The authors would like to thank JAXA for the PALSAR-2 data and Dr. Shimada in particular for ensuring that Ascension Island was imaged so very soon after the satellite was launched.

References

[1] X. Pi, "Ionospheric effects on spaceborne synthetic aperture radar and a new capability of imaging the ionosphere from space," *Space Weather*, vol. 13, no. 11, pp. 737–741, Nov. 2015.

[2] N. C. Rogers and S. Quegan, "The accuracy of Faraday rotation estimation in satellite synthetic aperture radar images," *IEEE Trans. Geosci. Remote Sens.*, vol. 52, no. 8, pp. 4799–4807, Aug. 2014.

[3] M. van de Kamp, P. S. Cannon, and M. Terkildsen, "Effect of the ionosphere on defocusing of space-based radars," *Radio Sci.*, vol. 44, no. 1, pp. 1–15, Feb. 2009.

[4] D. P. Belcher, "Theoretical limits on SAR imposed by the ionosphere," *IET Radar, Sonar Navigat.*, vol. 2, no. 6, pp. 435–448, Dec. 2008.

[5] D. P. Belcher and P. S. Cannon, "Ionospheric effects on synthetic aperture radar (SAR) clutter statistics," *IET Radar, Sonar Navigat.*, vol. 7, no. 9, pp. 1004–1011, Dec. 2013.

[6] D. P. Belcher and N. C. Rogers, "Theory and simulation of ionospheric effects on synthetic aperture radar," *IET Radar, Sonar Navigat.*, vol. 3, no. 5, pp. 541–551, Oct. 2009.

[7] C. R. Mannix, D. P. Belcher, P. S. Cannon, and M. J. Angling, "Using GNSS signals as a proxy for SAR signals: Correcting ionospheric defocusing," *Radio Sci.*, vol. 51, no. 2, pp. 60–70, Feb. 2016.

[8] M. M. J. L. van de Kamp, P. S. Cannon, and R. J. Watson, "V/UHF space radars: Spatial phase decorrelation of transionospheric signals in the equatorial region," *Radio Sci.*, vol. 45, no. 4, Aug. 2010.

[9] F. Meyer, R. Bamler, N. Jakowski, and T. Fritz, "The potential of low-frequency SAR systems for mapping ionospheric TEC distributions," *IEEE Geosci. Remote Sens. Lett.*, vol. 3, no. 4, pp. 560–564, Oct. 2006.

[10] X. Pi, A. Freeman, B. Chapman, P. Rosen, and Z. Li, "Imaging ionospheric inhomogeneities using spaceborne synthetic aperture radar," *J. Geophys. Res., Space Phys.*, vol. 116, no. A4, p. A04303, Apr. 2011.

[11] A. Rosenqvist, M. Shimada, N. Ito, and M. Watanabe, "ALOS PALSAR: A pathfinder mission for global-scale monitoring of the environment," *IEEE Trans. Geosci. Remote Sens.*, vol. 45, no. 11, pp. 3307–3316, Nov. 2007.

[12] D. P. Belcher, P. S. Cannon, and A. Gustavsson, "The Ascension Island experiment: Measurement of ionospheric scintillation effects on PALSAR-2," presented at the Int. Geosci. Remote Sens. Symp. (IGARSS), Milan, Italy, Jul. 2015, pp. 3191–3194, doi: 10.1109/IGARSS.2015.7326496.

[13] M. Shimada, O. Isoguchi, T. Tadono, and K. Isono, "PALSAR radiometric and geometric calibration," *IEEE Trans. Geosci. Remote Sens.*, vol. 47, no. 12, pp. 3915–3932, Dec. 2009.

[14] Y. Kankaku, Y. Osawa, S. Suzuki, and T. Watanabe, "The overview of the L-band SAR onboard ALOS-2," in *Proc. Prog. Electromagn. Res. Symp. (PIERS)*, Moscow, Russia, 2009, pp. 735–738.

[15] Y. Kankaku, S. Suzuki, and Y. Osawa, "ALOS-2 mission and development status," in *Proc. IEEE Geosci. Remote Sens. Symp. (IGARSS)*, Melbourne, VIC, Australia, Jul. 2013, pp. 2396–2399.

[16] C. L. Rino, "A power law phase screen model for ionospheric scintillation: 1. Weak scatter," *Radio Sci.*, vol. 14, no. 6, pp. 1135–1145, Nov./Dec. 1979.

[17] C. L. Rino, "On the application of phase screen models to the interpretation of ionospheric scintillation data," *Radio Sci.*, vol. 17, no. 4, pp. 855–867, Jul./Aug. 1982.

[18] E. Thébault *et al.*, "International geomagnetic reference field: The 12th generation," *Earth, Planets Space*, vol. 67, p. 79, May 2015.

[19] L. J. Nickisch, "A power law power spectral density model of total electron content structure in the polar region," *Radio Sci.*, vol. 39, no. 1, pp. 1–8, Feb. 2004, doi: 10.1029/2002RS002818.

[20] J. Aarons, "Global morphology of ionospheric scintillations," *Proc. IEEE*, vol. 70, no. 4, pp. 360–378, Apr. 1982.

[21] C. S. Carrano, K. M. Groves, and R. G. Caton, "A phase screen simulator for predicting the impact of small-scale ionospheric structure on SAR image formation and interferometry," presented at the IEEE Int. Geosci. Remote Sens. Symp. (IGARSS), Jul. 2010, pp. 162–165.

[22] E. J. Fremouw and J. A. Secan, "Modeling and scientific application of scintillation results," *Radio Sci.*, vol. 19, no. 3, pp. 687–694, May/Jun. 1984.

[23] S. Basu *et al.*, "250 MHz/GHz scintillation parameters in the equatorial, polar, and auroral environments," *IEEE J. Sel. Areas Commun.*, vol. 5, no. 2, pp. 102–115, Feb. 1987.

[24] N. C. Rogers, S. Quegan, J. S. Kim, and K. P. Papathanassiou, "Impacts of ionospheric scintillation on the BIOMASS P-band satellite SAR," *IEEE Trans. Geosci. Remote Sens.*, vol. 52, no. 3, pp. 1856–1868, Mar. 2014.

[25] S. Basu, S. Basu, E. Costa, C. Bryant, C. E. Valladares, and R. C. Livingston, "Interplanetary magnetic field control of drifts and anisotropy of high-latitude irregularities," *Radio Sci.*, vol. 26, no. 4, pp. 1079–1103, Jul./Aug. 1991.

[26] A. J. Van Dierendonck, J. Klobuchar, and Q. Hua, "Ionospheric scintillation monitoring using commercial single frequency C/A code receivers," in *Proc. 6th Int. Tech. Meet. Satellite Division Inst. Navigat. (ION GPS)*, Arlington, VA, USA, 1993, pp. 1315–1322.

[27] C. S. Carrano, K. M. Groves, W. J. McNeil, and P. H. Doherty, "Scintillation characteristics across the GPS frequency band," in *Proc. 25th Int. Tech. Meet. Satellite Division Inst. Navigat.*, Nashville, TN, USA, 2012, pp. 1972–1989.

[28] D. P. Belcher, C. R. Mannix, and P. S. Cannon, "Measurement of the ionospheric scintillation parameter CkL from SAR images of clutter," *IEEE Trans. Geosci. Remote Sens.*, vol. 55, no. 10, pp. 5937–5943, Oct. 2017, doi: 10.1109/TGRS.2017.2717081.

Christopher R. Mannix received the M.Sci. degree in physics and the Ph.D. degree in electronic, electrical and systems engineering from the University of Birmingham, Birmingham, U.K., in 2012 and 2016, respectively.

His research interests included the effects of the ionosphere on radar and navigation systems, as well as the use of synthetic aperture radar systems as an ionospheric measurement tool.

David P. Belcher received the B.Sc. degree in physics from Kings College London, London, U.K., in 1989, and the Ph.D. degree from University College, London, in 1997.

In 1989, he joined the Royal Signals and Radar Establishment (later DRA and DERA), Great Malvern, U.K., where he worked on high-resolution synthetic aperture radar (SAR) processing, including image distortion, inertial sensors, spotlight mode, and autofocus. He was the manager of the airborne low-frequency SAR program at DERA, and was then promoted to a Senior Scientist in 1998. In 2001, he joined Dstl, Great Malvern, U.K., where he led the U.K. radar team for several international collaborative projects in system-level space-based SAR and MTI. In 2005, he became a Dstl Associate Fellow individually funded for his work on space-based low-frequency SAR. In 2011, he joined the University of Birmingham, Birmingham, U.K., as a Co-Investigator, where he developed a theoretical description of the effects of ionospheric turbulence on space-based SAR, and designed an experiement to test his theory.

Paul S. Cannon received the B.Sc. degree in physics, the M.Sc. degree in electronics, and the Ph.D. degree in space radio physics from the University of Southampton, Southampton, U.K., in 1975, 1976, and 1981, respectively.

From 1979 to 1981, he was a Satellite Communications Engineer with Marconi Space and Defence Systems. From 1981 to 2001, he was a Research Scientist with the U.K. Ministry of Defense, London, U.K. In 2001, his laboratory was privatized to become a part of QinetiQ plc, Farnborough, U.K. In 2013, he joined the University of Birmingham, Birmingham, U.K., as a Professor of radio science and systems. His research interests include radio propagation and the radio environment impacts communications, radar, and navigation systems. He has made numerous personal and team contributions and his papers include those addressing ionospheric modification, high-frequency communications and radars, meteor scatter communications, and space radars.

Dr. Cannon serves on the government advisory committees, has been an Expert witness to a Parliamentary Select Committee, and has supported the Prime Minister's Committee on Science and Technology. He is currently the President of the International Union of Radio Science. He is a fellow of the Royal Academy of Engineering and was appointed to the Office of the Order of the British Empire by Her Majesty the Queen in 2014.